

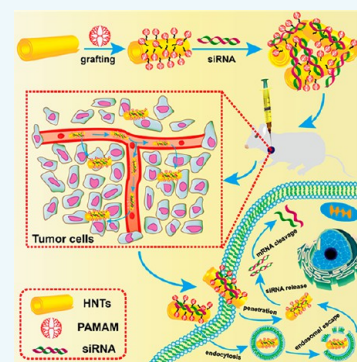
# Functionalization of Halloysite Nanotubes via Grafting of Dendrimer for Efficient Intracellular Delivery of siRNA

Zheru Long,<sup>†,‡</sup> Yan-Ping Wu,<sup>‡,‡</sup> Hua-Ying Gao,<sup>‡</sup> Yi-Fang Li,<sup>‡</sup> Rong-Rong He,<sup>\*,‡</sup> and Mingxian Liu<sup>\*,†,‡</sup>

<sup>†</sup>Department of Materials Science and Engineering and <sup>‡</sup>Guangdong Province Key Laboratory of Pharmacodynamic Constituents of TCM and New Drugs Research, College of Pharmacy, Jinan University, Guangzhou 510632, China

## Supporting Information

**ABSTRACT:** Here, polyamidoamine grafted halloysite nanotubes (PAMAM-g-HNTs) were synthesized for loading of siRNA in order to intracellular delivery of siRNA and treat of breast cancer via gene therapy. The successful grafting of PAMAM on HNTs was confirmed by various analytical methods. The size, zeta potential, and grafting ratio of PAMAM-g-HNTs is ~206.2 nm, +19.8 mV, and 3.04%, respectively. PAMAM-g-HNTs showed good cytocompatibility toward HUVECs (84.7%) and MCF-7 cells (82.3%) even at high concentration of 100  $\mu\text{g}/\text{mL}$ . PAMAM-g-HNTs/siRNA exhibited enhanced cellular uptake efficiency of 94.3% compared with Lipofectamine 2000 (Lipo2000)/siRNA (83.6%). PAMAM-g-HNTs/small interfering RNA-vascular endothelial growth factor (siVEGF) led to 78.0% knockdown of cellular VEGF mRNA and induced 33.6% apoptosis in the MCF-7 cells, which is also much higher than that of Lipo2000/siVEGF. In vivo anti-cancer results demonstrated that PAMAM-g-HNTs/siVEGF treated 4T1-bearing mice showed enhanced anti-cancer efficacy than Lipo2000/siVEGF group. Also, the nanocarrier system showed negligible toxic effects toward the major organs of mice. In vivo fluorescence imaging studies showed that there is a slight decrease in the fluorescence signal of PAMAM-g-HNTs/cy5-siVEGF after 72 h post-injection. Therefore, PAMAM-g-HNTs show promising application as novel nanovectors for siRNA delivery and gene therapy of cancer.



## INTRODUCTION

Gene therapy, a novel and efficient routine for treating tough diseases, has attracted extensive research interest worldwide. Among these efforts, RNA interference (RNAi) is considered a critical therapeutic approach which can regulate gene expression through sequence specific degradation of mRNA in eukaryotic cells.<sup>1,2</sup> Especially, small interfering RNA (siRNA) has been explored as a potential gene drug for treatment of various classes of hereditary and acquired diseases owing to its significant effects, high specificity, and minor side effects.<sup>3,4</sup> However, it is challenging to select a suitable vector for siRNA delivery in gene therapy. In the past several years, many viral and nonviral vectors have been designed for carrying siRNA.<sup>5,6</sup> Viral vectors are restricted in clinical use because of inflammatory reactions, high toxicity, strong immunogenicity, and many other inherent safety concerns. Nonviral carriers have caused more and more attractions owing to their good biocompatibility and proper physicochemical properties.<sup>7</sup> Inorganic nanoparticles, as promising nonviral carriers, containing fluorescent carbon nanoparticle (FCN),<sup>8</sup> gold nanoparticle (AuNP),<sup>9</sup> and graphene oxide (GO)<sup>10</sup> have been designed as nonviral vectors that offer commendable gene transfection efficiency. Generally, surface functionalization of these nanoparticles with cationic polymers is necessary for complexation of the negatively charged nucleic acid. For example, amino silanes, chitosan, polyethylenimine (PEI), and polyamidoamine (PAMAM) are commonly used to modify inorganic nanoparticles for siRNA delivery. Feng et al.

prepared PEGylated GO nanosheets combined with photo-thermal and gene therapy for promoting treatment effects toward pancreatic cancer.<sup>10</sup> AuNPs conjugated with PAMAM were also designed as nonviral transfection agents with optimized colloidal stability and enhanced transfection efficiency in vitro.<sup>9</sup> Selenium/ruthenium decorated metal organic frameworks (MOFs) were developed for treatment of breast cancer via delivery of pooled siRNAs.<sup>11</sup> PEI functionalized carbon nanotubes (CNTs)/siRNA could effectively induce apoptosis of tumor cells both in vivo and in vitro.<sup>12</sup> PAMAM-coated silica nanoparticles were also used for targeting and imaging of HER2-expressing cells.<sup>13</sup> However, inorganic nanoparticles from nature with satisfied cell uptake efficiency and good biosafety have rarely been studied as gene vectors.<sup>14,15</sup>

Halloysite nanotubes (HNTs), derived from natural clay deposits, show promise in applications in drug delivery. HNTs show a unique tubular nanostructure with outer diameter of 45–70 nm and inner diameter of 10–15 nm, and the chemical formula of HNTs is  $\text{Al}_2\text{Si}_2\text{O}_5(\text{OH})_4 \cdot n\text{H}_2\text{O}$ .<sup>16,17</sup> HNTs display many advantages in physicochemical properties such as high dispersion stability, good biocompatibility, high reactivity, and proper nanoscale dimensions for application in drug delivery.<sup>17–19</sup> HNTs contain hydroxyl groups on their surfaces

Received: May 10, 2018

Revised: June 24, 2018

Published: June 27, 2018

for modification and conjugation of drugs. HNTs have been reported able to be successfully loaded with therapeutic drugs, antibacterial agents, nucleic acids, and antioxidants.<sup>20–25</sup> Massaro et al. found that curcumin chemically conjugated HNTs have a dual stimuli-responsive ability when exposed to glutathione (GSH)-rich or acidic environment.<sup>26</sup> Fakhrullin et al. prepared dextrin-coated HNTs for enzyme-activated intracellular delivery of brilliant green for anti-cancer treatment.<sup>27</sup> Yuan et al. used 3-aminopropyltriethoxysilane (APTES)-modified HNTs to load and release ibuprofen with increased drug loading capacity.<sup>28</sup> In our previous work, we designed chitosan-grafted HNTs and chitosan oligosaccharide-grafted HNTs as curcumin or doxorubicin carriers to enhance the anti-cancer efficacy.<sup>29,30</sup> For gene delivery, APTES functionalized HNTs were used as carriers to deliver the antisense oligonucleotides toward HeLa cells.<sup>14</sup> Short HNTs grafted with PEI (PEI-g-HNTs) were prepared for the enhancement of transfection efficiency in human normal cells and tumor cells.<sup>31</sup> Very recently, HNTs functionalized with PAMAM dendrimer have been designed as a vector of therapeutic compounds.<sup>32</sup> Therefore, functionalized HNTs are considered novel and promising nanovehicles for gene delivery in the treatment of tumors.

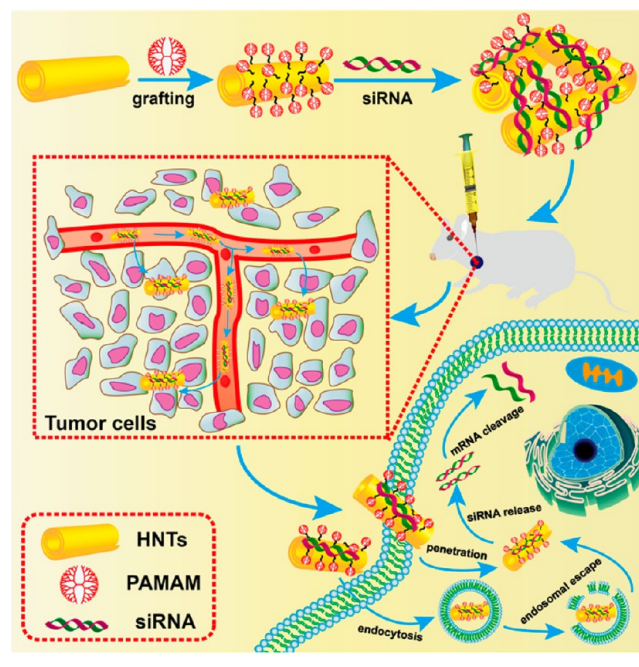
Although PEI-g-HNTs showed considerable transfection efficiency toward tumor cells, the cytotoxicity of complexes would limit its progressive application in gene therapy. Besides, it is still uncertain how the modified HNTs will perform in the specific cancer therapy in vivo. In the present work, we proposed PAMAM-g-HNTs to load siRNA and reduce the expression of the VEGF gene in breast cancer cells. The morphological and chemical analyses of PAMAM-g-HNTs demonstrated the grafting of polymer on surfaces of HNTs. PAMAM-g-HNTs showed good cytocompatibility, and PAMAM-g-HNTs/siRNA complexes possessed high cellular uptake efficiency toward MCF-7 cells. The animal model of 4T1-bearing mice experiments demonstrated that PAMAM-g-HNTs/siVEGF had a better effect of inhibiting tumor growth than Lipo2000/siVEGF. As shown in Scheme 1, PAMAM-g-HNTs can bind siRNA and the complex can be taken up by the tumor cells for down-regulating the expression level of VEGF mRNA in tumor cells.

## RESULTS AND DISCUSSION

### Preparation and Characterization of PAMAM-g-HNTs.

Figure 1A illustrates the preparation methods of PAMAM-g-HNTs. APTES was reacted with the hydroxyl groups on HNTs to obtain HNTs-NH<sub>2</sub>. Then, HNTs-COOH were obtained by the reaction of HNTs-NH<sub>2</sub> with SA. Finally, PAMAM-g-HNTs were prepared through the reaction of amino groups on PAMAM and HNTs-COOH. As shown in Figure 1B, the evidence of the existence of the PAMAM on HNTs was examined by XPS analysis. Wide scans and high-resolution XPS of nitrogen (N 1s) and carbon (C 1s) spectra were analyzed. The peaks of C–N (285.63 eV) and C=O (287.28 eV) derived from the PAMAM appear in the carbon (C 1s) spectra of PAMAM-g-HNTs. Besides, the peak of N–H bond (401.10 eV) in the nitrogen (N 1s) spectrum is attributed to the NH<sub>2</sub> groups of PAMAM.<sup>33</sup> From the FT-IR analysis of HNTs and PAMAM-g-HNTs (Figure 1C), the new peak at 1548 cm<sup>-1</sup> is due to the N–H deformation and C–N stretching combination band of amide II bands.<sup>34,35</sup> Figure 1D compares the differences of HNTs and modified HNTs in XRD patterns. The shielding effect by grafting of PAMAM on

**Scheme 1. Schematic Illustration for the Preparation of PAMAM-g-HNTs/siRNA Complex and Its Intracellular Process in Tumor Cells**



HNTs results in the decrease of diffraction peak of HNTs at  $\sim 12^\circ$ .<sup>31</sup>

As shown in Figure 2A, the average hydrodynamic diameter ( $R_h$ ) of HNTs is  $\sim 202.3$  nm (PDI = 0.239), while PAMAM-g-HNTs possess an average diameter of  $\sim 206.2$  nm (PDI = 0.253), which is 3.9 nm larger than HNTs. DLS is usually applied to evaluate the size of the spherical particle. However, HNTs are long cylinders with high aspect ratio, so the DLS cannot reflect the single dimension of HNTs identically but rather to a reference value. The DLS size difference between HNTs and PAMAM-g-HNTs means PAMAM has been grafted onto HNTs rather than illustrating the layer of PAMAM polymer on HNTs is  $\sim 4$  nm thickness. Previous study has also reported the similar size difference between HNTs and modified HNTs by DLS analysis, but there is also a small morphological difference between them.<sup>36</sup> From zeta potential results (Figure 2B), a totally different zeta potential can be seen for HNTs and PAMAM-g-HNTs. HNTs show a negative zeta potential ( $-18.6$  mV) while PAMAM-g-HNTs are positively charged ( $+19.8$  mV). As a comparison, the zeta potential of HNTs-NH<sub>2</sub> and HNTs-COOH is  $+36.6$  mV and  $-18.4$  mV, respectively (Figure S1). Figure 2C compares the TGA curves of HNTs and PAMAM-g-HNTs. PAMAM-g-HNTs show a 22.6% weight loss upon heating to  $700^\circ\text{C}$ , while the weight loss of HNTs is 20.2%. The calculated polymer grafting ratio is  $\sim 3.04\%$ . The percent of PAMAM grafting onto HNTs was also determined by 2,4,6-trinitrobenzenesulfonic acid (TNBS) assay (Supporting Information), and the estimated grafting of primary amines of PAMAM onto HNTs is  $\sim 7.9\%$  from TNBS assay. Figure S2 shows the pore distribution of PAMAM-g-HNTs. The surface defects of HNTs at 3 nm disappear after PAMAM grafting.<sup>37</sup> Besides, the pore volume curve of PAMAM-g-HNTs is below that of HNTs, which suggests that HNTs are wrapped by PAMAM. From the AFM images (Figure 2D), no obvious shape difference is identified between PAMAM-g-HNTs and

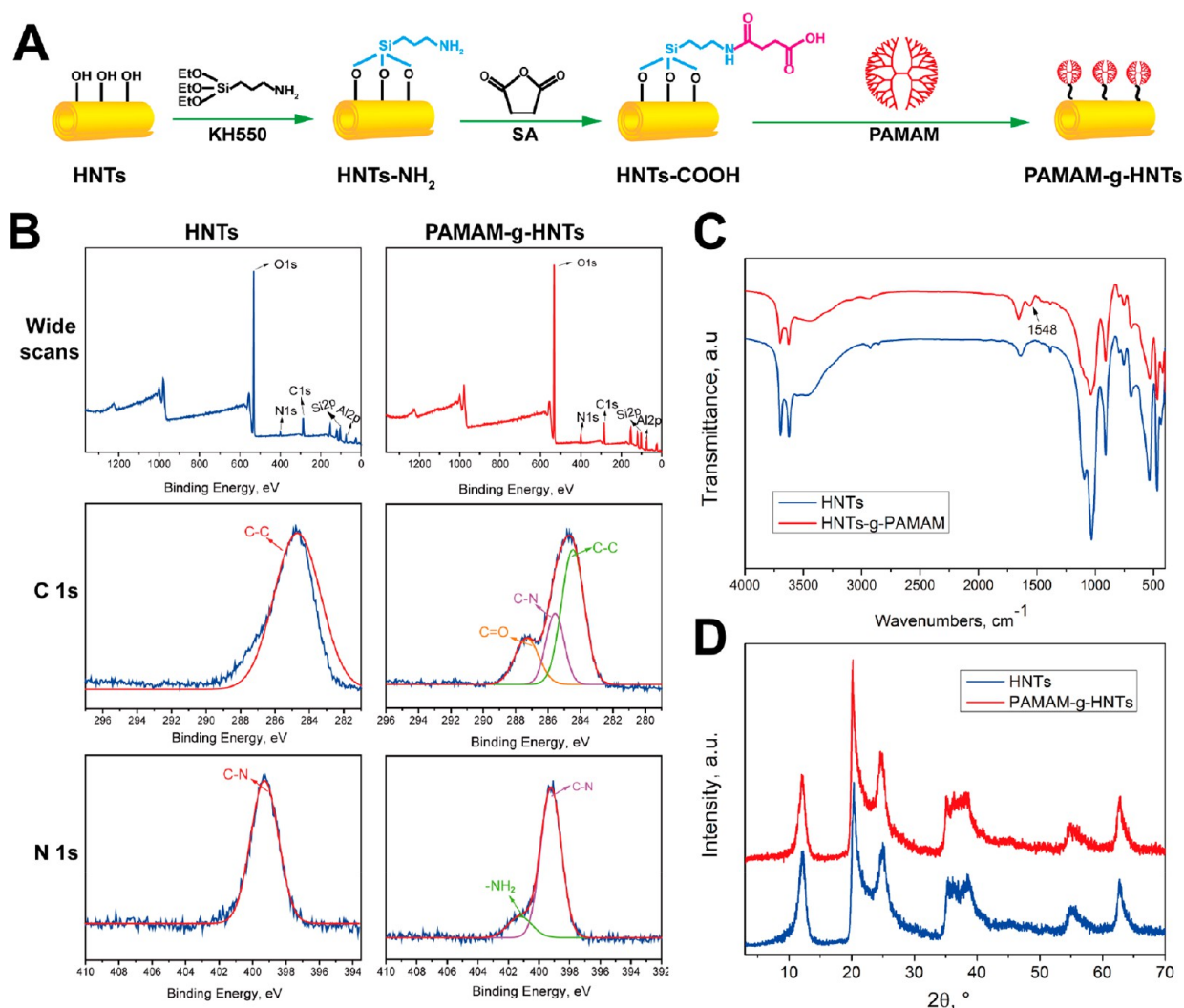


**Figure 1.** (A) Synthesis processes of PAMAM-g-HNTs. (B) XPS wide scans and C 1s, N 1s high-resolution scanning spectra, (C) FT-IR, and (D) XRD analysis of HNTs and PAMAM-g-HNTs.

HNTs. Similarly, they display characteristic tubular structure with hollow lumen in TEM images (Figure 2E), which demonstrates that the tubular structure of HNTs is reserved after grafting.<sup>30,38</sup> In addition, a black layer of PAMAM polymer is located on the surfaces of HNTs, which illustrates the successful grafting modification of HNTs.<sup>39</sup>

**siRNA Binding of PAMAM-g-HNTs, Cytotoxicity, and Cellular Uptake.** As shown above, PAMAM-g-HNTs exhibit positively charged surfaces, which enable complexation with negatively charged siRNA, showing potential application in gene vectors. The condensation capability of PAMAM-g-HNTs with siRNA was examined by agarose gel electrophoresis. As shown in Figure 3A, PAMAM-g-HNTs can bind siRNA completely at the weight ratio of 20. PAMAM-g-HNTs show high siRNA binding abilities and are an effective gene-delivery vector. CCK-8 assay was employed to evaluate the cytotoxicity of PAMAM-g-HNTs. As represented in Figure 3B, the cytotoxicity of PAMAM-g-HNTs toward HUVECs and MCF-7 cells show a gradual increase with the increase in nanoparticle concentration. Both the cell viability of HUVECs and MCF-7 cells remains above 80% even when the concentration of PAMAM-g-HNTs increases to 100  $\mu\text{g}/\text{mL}$ . However, with the increase in concentration of HNTs, the cell

viability decreases. Previous research suggests that dendrimers such as PAMAM have an intrinsic cell toxicity, which limits its application in biological systems.<sup>40,41</sup> Previous study has shown that the toxicity of cationic polymers toward cells would decrease after chemical linking with nanoparticles, which is due to the decreased cationic group density brought by nanoparticle immobilization.<sup>42</sup> For example, PAMAM grafted gold nanoparticles were used as nonviral transfection agent for DNA because of its low cytotoxicity and suitable transfection efficacy.<sup>9</sup> Similarly, the cytotoxicity of PAMAM is also lowered by the grafting of PAMAM on HNTs. The high siRNA condensation ability and low cytotoxicity of PAMAM-g-HNTs demonstrate that it is a potential gene delivery candidate in biological application.

Cellular uptake efficiency of nanoparticles depends on diverse of physiochemical properties, such as morphology, zeta potential, particle size, as well as physiological stability.<sup>43</sup> The cellular uptake efficiency of PAMAM-g-HNTs is related to many factors including optimal concentration of siRNA and appropriate PAMAM-g-HNTs/cy3-siRNA weight ratios. Figure 3C shows the statistical cell counts by flow cytometry when treated with various siRNA concentrations at the PAMAM-g-HNTs/cy3-siRNA weight ratio of 80. It can be seen from

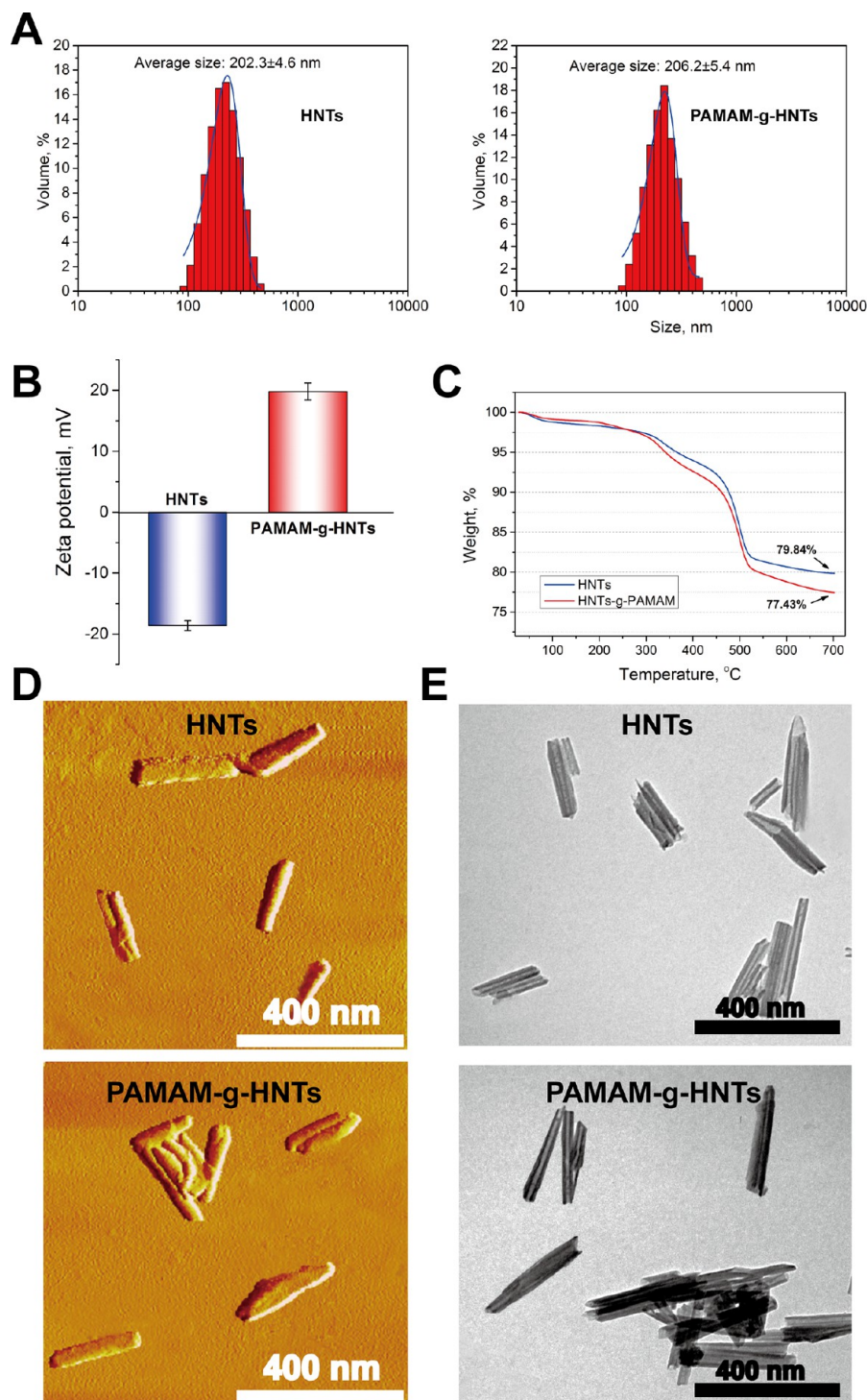


**Figure 2.** (A) DLS size analysis, (B) zeta potential, and (C) thermogravimetric analysis, (D) AFM images, and (E) TEM photos of HNTs and PAMAM-g-HNTs.

Figure 3D that the optimal uptake efficiency (94.3%) of PAMAM-g-HNTs/cy3-siRNA is achieved when the siRNA concentration is 60 nM, which is larger than that of Lipo2000/cy3-siRNA siRNA complexes (83.6%). The influence of weight ratios of PAMAM-g-HNTs/siRNA complexes on cellular uptake efficacy was then investigated. As exhibited in Figure 3E, the numbers of cy3-siRNA positive cells increase with the increase of vector/siRNA weight ratios. Figure 3F shows the statistical cell counts by flow cytometry when treated with a series of weight ratios of PAMAM-g-HNTs/cy3-siRNA. As

displayed in Figure 3G, PAMAM-g-HNTs/cy3-siRNA show an increasing cellular uptake level with the increase in weight ratios, and the optimal uptake level (94.3%) is achieved at the weight ratio of 80. The uptake level of PAMAM-g-HNTs/cy3-siRNA complexes is also related to the stability of complexes. A premature disassembly of the complexes during cell internalization can reduce cellular uptake efficiency.<sup>43</sup> The large surface area of PAMAM-g-HNTs with surface pore structure increases the contact areas with siRNA, which ensures the highly efficient loading of siRNA.

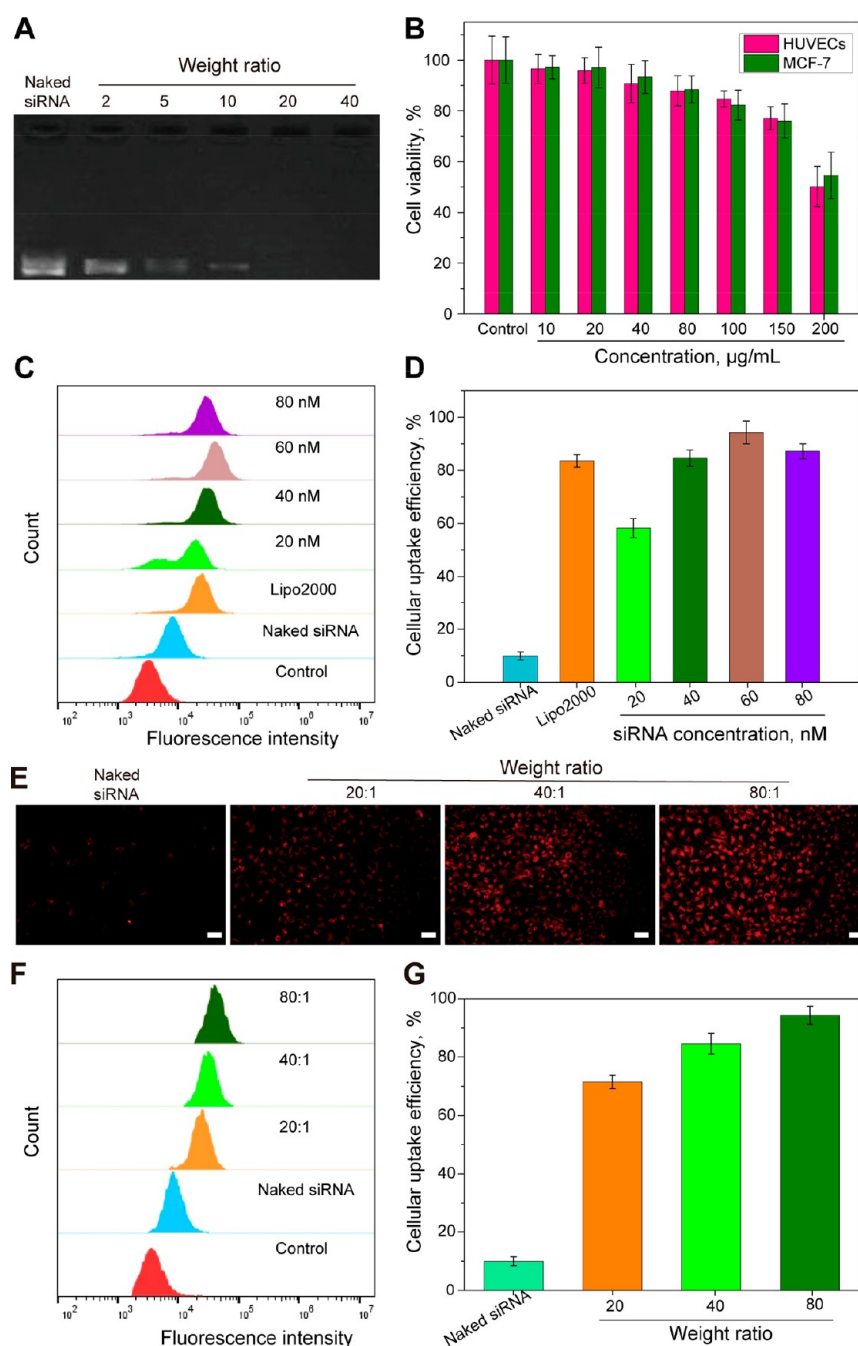


**Figure 3.** (A) Agarose gel electrophoresis assay of PAMAM-g-HNTs/siRNA at various weight ratios. (B) Cell viability of HUVECs and MCF-7 cells after incubated with the PAMAM-g-HNTs at different concentrations ( $n = 4$ ) for 24 h. Flow cytometry evaluations of the transfection efficiencies of MCF-7 cells treated with different siRNA concentrations at the PAMAM-g-HNTs/siRNA weight ratio of 80. (C) Statistical cell counts by flow cytometry, where the  $y$ -axis represents cell counts and the  $x$ -axis represents the cy3 fluorescence intensities, respectively. (D) Cellular uptake level of PAMAM-g-HNTs/cy3-siRNA (weight ratio = 80) in MCF-7 cells at various siRNA concentrations. (E) Fluorescent photos, (F) flow cytometry analysis, and (G) cellular uptake efficiency of PAMAM-g-HNTs/siRNA complexes at different weight ratios in MCF-7 cells. Scale bars = 80  $\mu\text{m}$ .

**Endosomal/Lysosomal Escape.** The efficacy of gene therapy largely depends on endosomal/lysosomal escape.<sup>8</sup> CLSM was used to examine the endosomal/lysosomal escape of siRNA (Figure 4). Nearly all the red fluorescence of cy3-siRNA is covered by the lysosome tracker green in cells after incubation with complexes for 4 h, which indicates that PAMAM-g-HNTs/cy3-siRNA complexes are internalized by cell lysosomes. The green (LysoTracker green) is separated from the red (cy3-siRNA) fluorescence after 6 h, which

demonstrates that cy3-siRNA escapes from the lysosome successfully. This phenomenon indicates that the PAMAM-g-HNTs/cy3-siRNA promote the escape of the cy3-siRNA from endosome/lysosome. Similar siRNA release following cellular uptake was also found in bioreducible fluorinated peptide dendrimer/siRNA complex and selenium nanoparticle modified metal organic frameworks/siRNA complex.<sup>11,43</sup>

**In Vitro VEGF Gene Silencing.** VEGF plays a key role in the angiogenesis of tumors.<sup>44</sup> The abnormal blood vessel

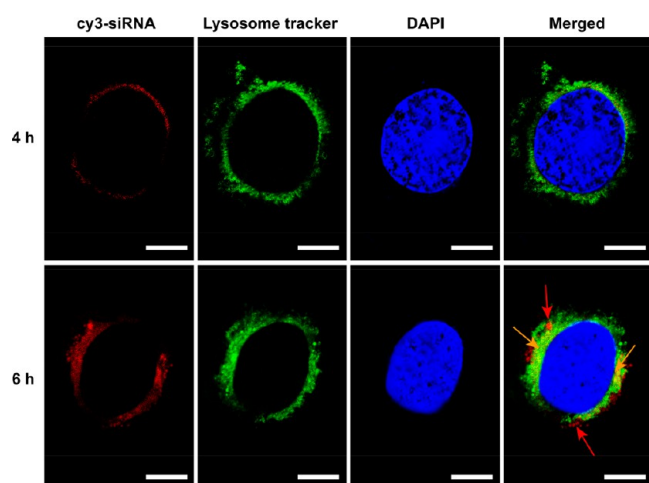


**Figure 4.** CLSM observation of siRNA escaped from endosome/lysosome. Cy3-siRNA (red); lysosome tracker (green); DAPI (blue). Scale bars = 20  $\mu\text{m}$ .

formation usually occurred by disruption of the VEGF gene, which controls the tumor growth as well as metastasis. However, the occurrence of the VEGF gene is different in tumor cells. The transcripts per million (TPM) of VEGF gene expression in MCF-7 cells is 23.9.<sup>45</sup> Hence, using small interfering RNA-vascular endothelial growth factor (siVEGF) to inhibit the expression of VEGF gene is considered an effective way to suppress tumor growth.<sup>46</sup>

The VEGF mRNA in MCF-7 cells was investigated by qRT-PCR. As presented in Figure 5A, compared with control group (phosphate buffered saline, PBS), the level of VEGF mRNA expression in MCF-7 cells shows  $\sim 78.0\%$  reduction after incubation with the PAMAM-g-HNTs/siVEGF. By comparison, the expression of VEGF mRNA in the PAMAM-g-HNTs/Scram, siVEGF, and Lipo2000/siVEGF groups is decreased by 11.9%, 19.1%, and 43.9%, respectively. From these results, it can be concluded that PAMAM-g-HNTs/siVEGF complexes can enhance cellular uptake of siVEGF and gene silencing efficiency in MCF-7 cells. The VEGF gene silencing efficacy of PAMAM-g-HNTs/siVEGF complexes was further confirmed by Western blot analysis (Figure 5B,C). The relative VEGF protein expression levels are 93.6%, 78.8%, 64.0%, 54.0%, and 23.9%, corresponding to the control, PAMAM-g-HNTs/Scram, siVEGF, Lipo2000/siVEGF, and PAMAM-g-HNTs/siVEGF complexes treated group, respectively. The PAMAM-g-HNTs/siVEGF show the most efficient reduction of VEGF protein expression in cells among the groups. The assessments are in line with the qRT-PCR assay. Both the qRT-PCR and Western blot assay confirm that the PAMAM-g-HNTs/siVEGF complexes can result in inhibition of VEGF gene expression in MCF-7 cells and be potentially applied as cancer gene therapy platform.

**Cell Apoptosis Assay.** AO/EB staining assay was designed to confirm cell apoptosis results in MCF-7 cells after treatment with different complexes. As shown in Figure 6A, MCF-7 cells show maximum apoptosis (orange cells) after treatment with PAMAM-g-HNTs/siVEGF. In contrast, Lipo2000/siVEGF complexes exhibit a better cell condition and fewer orange cells in the fluorescence image. This result suggests that PAMAM-g-HNTs/siVEGF can induce more cell apoptosis than Lipo2000/siVEGF. The Annexin V-FITC apoptosis detection kit was further applied to evaluate the efficacy of

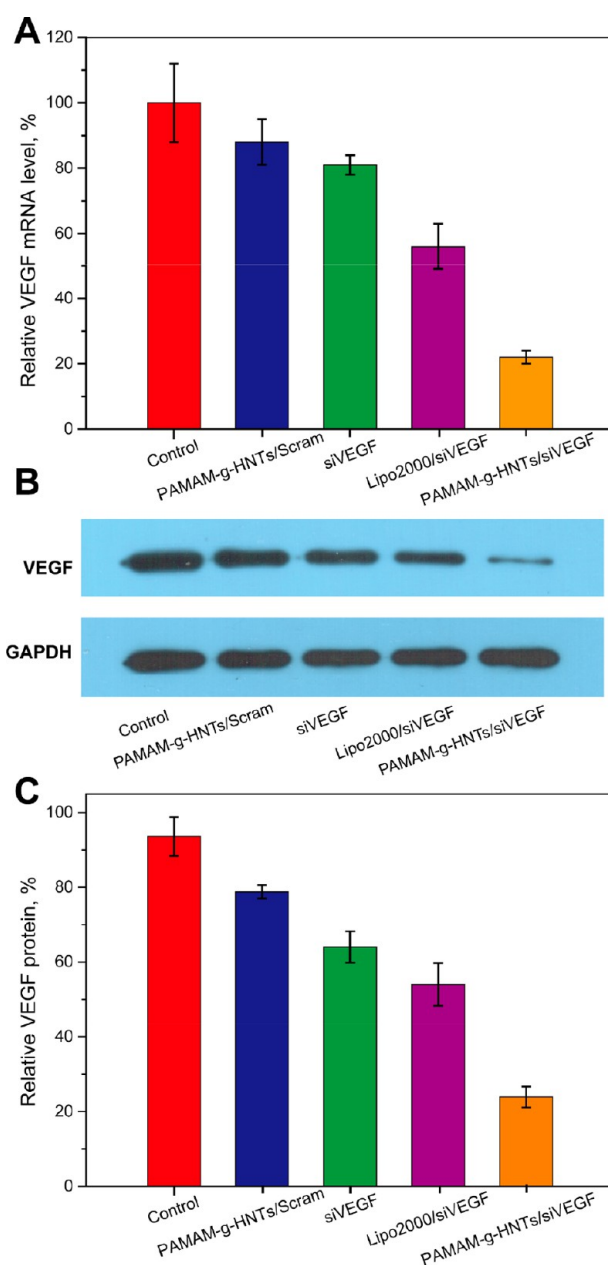


**Figure 5.** Determination of (A) VEGF mRNA levels and (B) VEGF protein expression in MCF-7 cells after treatment with different complexes by qRT-PCR analysis and Western blot assay. (C) Quantitative detection of VEGF protein expression in MCF-7 cells.

VEGF gene down-regulation in MCF-7 cells using flow cytometry. As shown in Figure 6B, the PAMAM-g-HNTs/siVEGF complexes result in 33.6% cell apoptosis (Q2+Q3) in MCF-7 cells. In contrast, control, PAMAM-g-HNTs/Scram, and siVEGF groups show less than 14.3% cell apoptosis ratio. In contrast, Lipo2000/siVEGF only induce 24.1% cell apoptosis. This result indicates that PAMAM-g-HNTs/siVEGF can regulate the VEGF gene expression and induce considerable tumor cell apoptosis.

**In Vivo Antitumor Efficacy of PAMAM-g-HNTs/siVEGF in 4T1-Bearing Mice.** To further confirm the efficiency and safety of PAMAM-g-HNTs/siVEGF in cancer treatment, the antitumor effect of PAMAM-g-HNTs/siVEGF was investigated in 4T1-bearing mice in vivo. During this experiment, mice were weighed every day (Figure 7A) and tumor volume

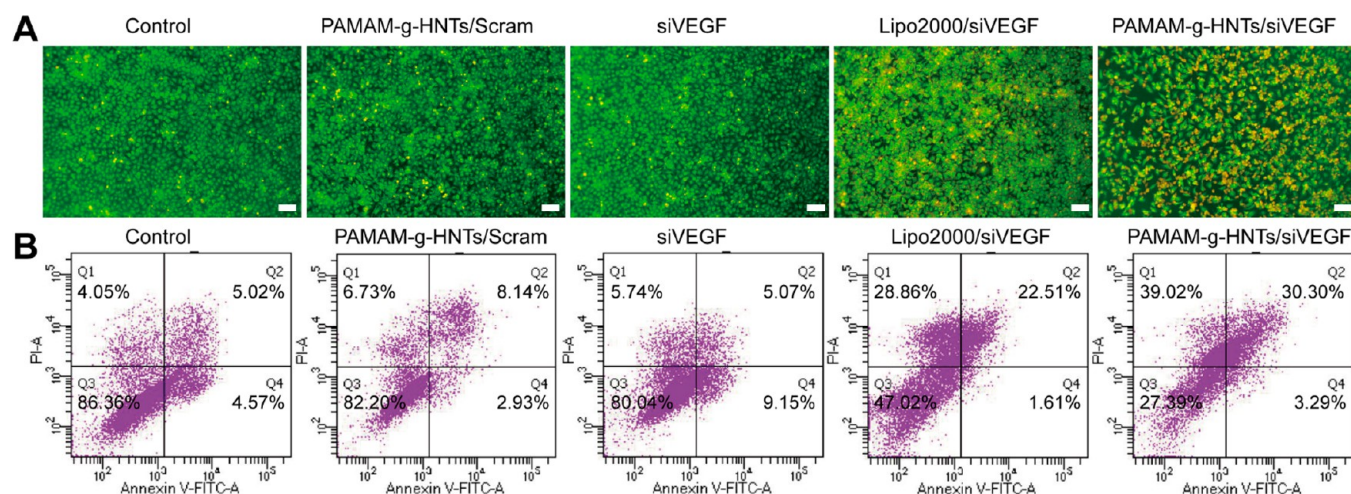


**Figure 6.** (A) Fluorescence photos of MCF-7 cells after treatment with AO/EB. (B) Induction of MCF-7 cell apoptosis after treatment with different siRNA formulations. Scale bars = 80  $\mu\text{m}$ .

of each mouse was also calculated every 3 days to reflect the tumor growth (Figure 7B). There is no obvious influence on body weight among different treatments (Figure 7A). It is noted that PAMAM-g-HNTs/siVEGF significantly reduced the tumor volume when compared to PAMAM-g-HNTs/Scram and siVEGF groups. PAMAM-g-HNTs/Scram and siVEGF groups have no significant effect in comparison with the control treatment. In particularly, the average tumor volume of the control group on day 15 is 477.9  $\text{mm}^3$ , while the average tumor volume of Lipo2000/siVEGF and PAMAM-g-HNTs/siVEGF on day 15 is 164.9 and 110.4  $\text{mm}^3$ , respectively. At the end of this experiment, 4T1 solid tumors of mice treated with different formulations were excised, photographed, and weighed. As shown in Figure 7C and D, PAMAM-g-HNTs/Scram and siVEGF treated groups have no significant change in tumor weight when compared with the control groups. However, the tumor weight is significantly decreased in Lipo2000/siVEGF and PAMAM-g-HNTs/siVEGF treatments with a high tumor inhibition rate at 38.3% and 55.1%, respectively. As expected, PAMAM-g-HNTs/siVEGF treatments show a higher tumor inhibition rate than Lipo2000/siVEGF treatment in 4T1-bearing mice. The antitumor effect presented in Figure 7C and D is consistent with the inhibition curves in Figure 7B. Besides, the antitumor effect in our study is similar to the previous research in which bioreducible fluorinated peptide dendrimers exhibited a more excellent in vivo antitumor effect than Lipo2000.<sup>43</sup> Therefore, the result indicates that PAMAM-g-HNTs/siVEGF treatment not only has a significant antitumor effect during the cancer therapy, but also has a better antitumor effect than Lipo2000/siVEGF treatment. It is confirmed the result in vitro that PAMAM-g-HNTs/siRNA show higher cellular uptake efficiency (94.3%) than Lipo2000/cy3-siRNA (83.6%). The large surface area of PAMAM-g-HNTs with surface pore structure increases the contact areas with siRNA, which highly enhances the efficient siRNA condensation and the uptake efficiency. The high uptake efficiency can contribute to the enhanced antitumor effect of PAMAM-g-HNTs/siVEGF in mice.

Subsequently, the histological analysis of tumor, heart, spleen, lung, and kidney in mice were detected by H&E staining. The representative photographs in Figure 7E show that PAMAM-g-HNTs/siVEGF induces more tumor necrosis than other treatments. Besides, PAMAM-g-HNTs/siVEGF

groups show no significant toxicity to major organs, while Lipo2000/siVEGF treatment displays certain tissue damage in tissue (indicated by the yellow arrows in Figure 7E). The toxicity of Lipo2000 in mice is related to its high surface charges. In total, it can be concluded that PAMAM-g-HNTs/siVEGF has provided an effective anti-cancer treatment without any obvious toxic effects to major organs. The lower toxicity effect of PAMAM-g-HNTs/siVEGF in mice is a result of HNTs decreasing the cationic group density of PAMAM. The excellent performance of the PAMAM-g-HNTs-based delivery system is related to the enhancement of gene transfection efficiency in vivo. It will be further confirmed in the following study.

**VEGF Gene Silencing Efficacy of PAMAM-g-HNTs/siVEGF on Tumor Tissues in 4T1-Bearing Mice.** The cationic polymer can easily form a complex with siRNA.<sup>47</sup> It has been reported that PEI modified CNTs could result in higher gene-silencing effects with low cytotoxicity.<sup>48–50</sup> Similar to PEI, PAMAM was also designed as a nonviral delivery vector for efficient siRNA delivery.<sup>51</sup> PAMAM can modify the selenium nanoparticles for better gene-silencing effects.<sup>52</sup> In this work, the excised tumor tissues were handled and the VEGF mRNA and protein levels were investigated for evaluating the relations between the tumor inhibition and the VEGF gene silencing. As shown in Figure 8A and B, VEGF protein expression in PAMAM-g-HNTs/siVEGF and Lipo2000/siVEGF groups were remarkably down-regulated. Besides, PAMAM-g-HNTs/siVEGF treatments have a better inhibition effect than Lipo2000/siVEGF treatment. The relative VEGF mRNA level also displays a similar silencing efficacy to protein expression in each group (Figure 8C). Furthermore, the expression of VEGF in tumor tissue was also detected by immunohistochemistry staining analysis. The brown area (the yellow arrow) in the representative photograph of tumor sections represented the high VEGF expression in tumor tissue (Figure 8D,E). The relative density of VEGF in the tumor section indicates that mice treated with PAMAM-g-HNTs/siVEGF show a significant reduction in VEGF expression. In particular, PAMAM-g-HNTs/siVEGF treatments show that VEGF expression level of 48.9% which is 39.4%, 26.4%, and 15.2% less than that of PAMAM-g-HNTs/Scram, siVEGF, and Lipo2000/siVEGF treatment, respec-

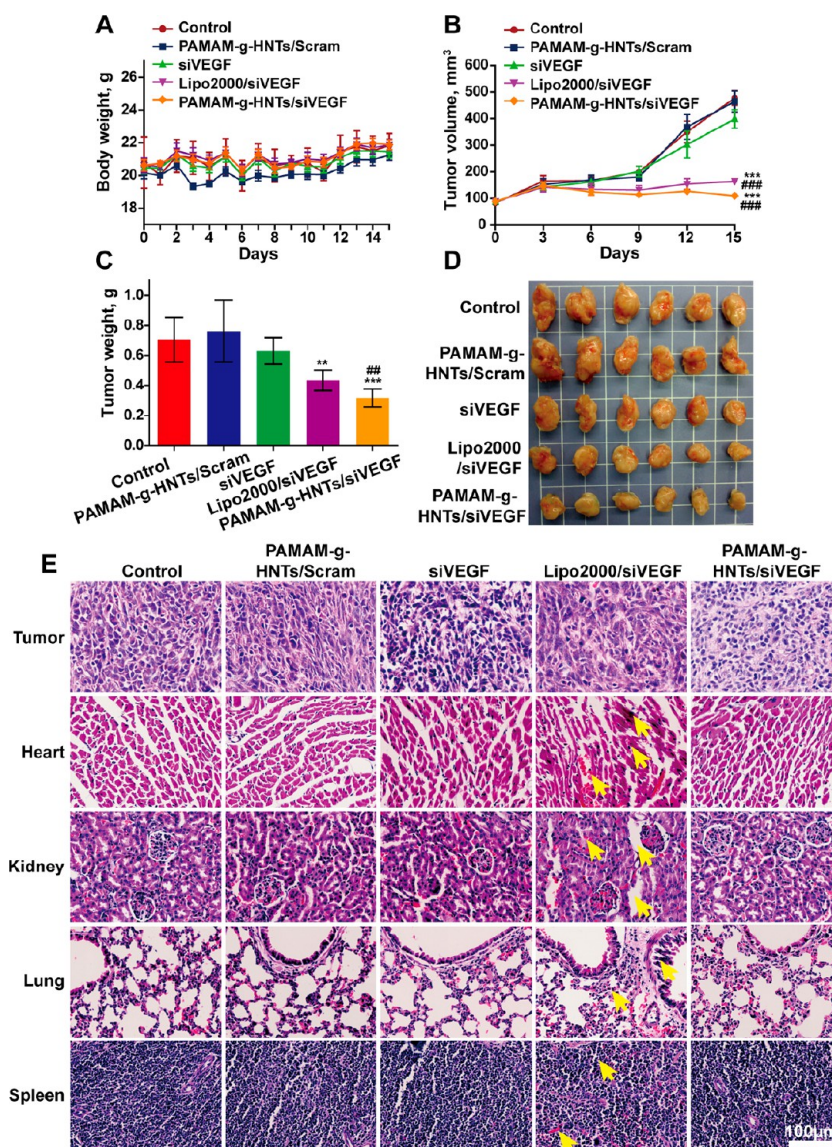


**Figure 7.** (A) Body weight, (B) tumor volume, (C) tumor weight, (D) photograph of excised 4T1 solid tumors, and (E) H&E staining of tumor, heart, kidney, lung, and spleen of mice. Mice were treated with saline, PAMAM-g-HNTs/Scram, siVEGF, Lipo2000/siVEGF, and PAMAM-g-HNTs/siVEGF (0.7 mg of siVEGF equiv/kg) via intratumoral injection. The arrows in the images of heart, kidney, and lung indicate tissue damage. The scale bars represent 100  $\mu\text{m}$ . The data were showed by mean  $\pm$  SD ( $n = 6$ ). \*\* $P < 0.01$ , \*\*\* $P < 0.001$  vs PAMAM-g-HNTs/Scram, ### $P < 0.01$ , #### $P < 0.001$  vs siVEGF.

tively. These results indicate that PAMAM-g-HNTs/siVEGF possesses an efficient VEGF silencing effect in vivo.

VEGF gene is indispensable during the period of angiogenesis in tumor growth and metastasis,<sup>53,54</sup> and the increase of tumor apoptosis is related to the decrease of tumor angiogenesis.<sup>55</sup> Therefore, we postulate that the excellent antitumor effect of PAMAM-g-HNTs/siVEGF is related to the VEGF silencing efficiency, which can increase tumor apoptosis by inhibiting tumor angiogenesis. In order to illustrate this point, apoptosis index in tumor tissue of 4T1-bearing mice was examined by TUNEL. As shown in Figure 8D and F, the brown spots (the red arrows) represent the apoptosis in tumor tissue. Compared with the PAMAM-g-HNTs/Scram group, the tumor tissue of both the PAMAM-g-HNTs/siVEGF group and Lipo2000/siVEGF group showed significant apoptosis. In all, PAMAM-g-HNTs/siVEGF can induce apoptosis and result in enhanced antitumor efficacy in breast cancer.

#### Control-Released Effect of PAMAM-g-HNTs/siVEGF in 4T1-Bearing Mice.

The results in vitro and the outstanding anti-tumor efficiency of PAMAM-g-HNTs/siVEGF in 4T1-bearing mice in vivo support RNAi-based cancer therapy. The controlled release effect of cy5-siVEGF was monitored by an in vivo imaging system after cy5-siVEGF, Lipo2000/cy5-siVEGF, and PAMAM-g-HNTs/cy5-siVEGF was administered intratumorally in 4T1-bearing mice. As shown in Figure 9A and B, the fluorescence intensities are equal at 3 h after injection, which implies that all formulations successfully enter the tumor tissues. The fluorescence signals (cy5-siVEGF) were reduced with time. It is notable that the fluorescence intensity is decreased slightly in PAMAM-g-HNTs/cy5-siVEGF groups, while cy5-siVEGF and Lipo2000/cy5-siVEGF groups show a significant reduction at 72 h post-injection, which agrees with the previous research.<sup>43</sup> The quantitative fluorescence intensity in tumor tissues suggests that nearly all PAMAM-g-HNTs/cy5-siVEGF accumulate in the tumor sites, while the free cy5-

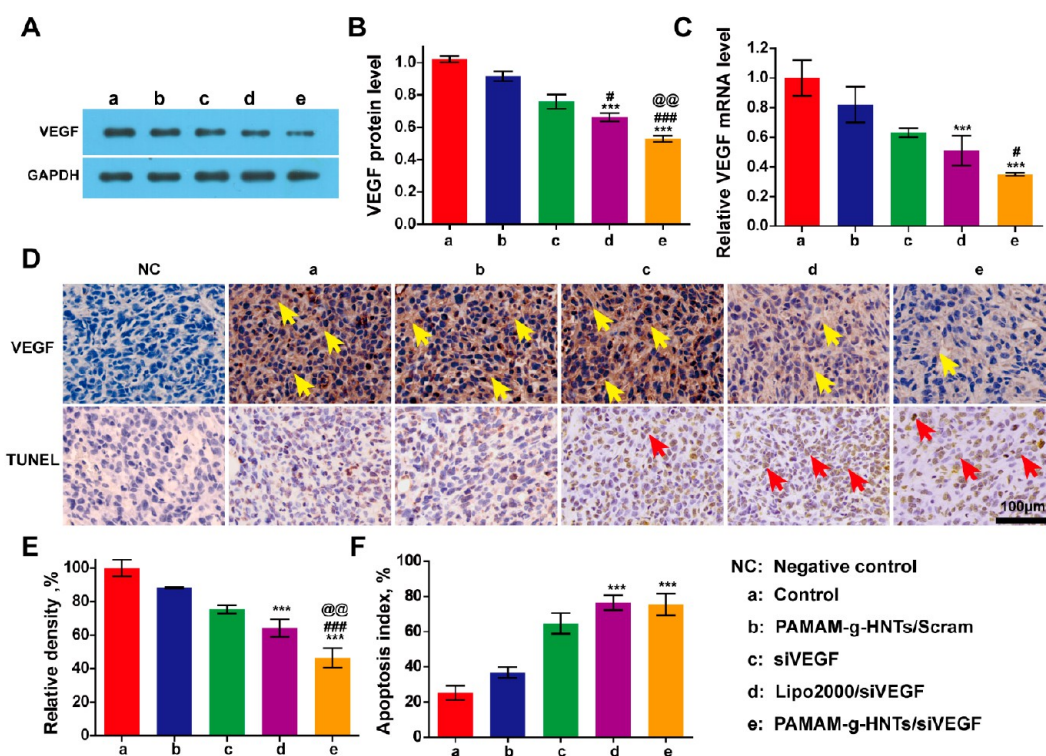


**Figure 8.** VEGF gene silencing efficacy of PAMAM-g-HNTs/siVEGF in vivo. (A–C) Protein expression and relative mRNA level of VEGF in tumor tissue. (D) Photographs of tumor sections examined by IHC and TUNEL assay. Yellow arrows represented the VEGF positive staining, and brown spot represented the TUNEL-positive cell nuclei. Scale bar is 100  $\mu\text{m}$ . (E) Relative density of VEGF-positive in tumor tissues in various groups was calculated by ImageJ software. (F) Apoptosis cell number counted in five random fields in a blind manner. The values were represented as mean  $\pm$  SD \*\*\* $P < 0.001$  vs PAMAM-g-HNTs/Scram. # $P < 0.05$ , ## $P < 0.01$ , ### $P < 0.001$  vs siVEGF; @@ $P < 0.01$  vs Lipo2000/siVEGF.

siVEGF and Lipo2000/cy5-siVEGF are rapidly excreted by the mice. It is supposed that PAMAM-g-HNTs/cy5-siVEGF may have a better enhanced permeability and retention (EPR) effect than other complexes in tumor, which leads to controlled drug released behavior.<sup>56</sup> The suitable size ( $\sim 200$  nm) and zeta potential ( $\sim +20$  mV) of carriers provide enhanced EPR effect.<sup>43</sup> In contrast, the high surface charge of Lipo2000 results in limited serum resistance and inefficient cellular internalization.<sup>57</sup> In all, it can be concluded that PAMAM-g-HNTs/siVEGF exhibit an excellent anti-tumor effect due to its enhanced gene transfection efficiency for inhibiting angiogenesis in tumor growth with lower toxicity and a good controlled gene release in tumor.

## EXPERIMENTAL PROCEDURES

**Materials.** HNTs were provided by Guangzhou Runwo Materials Technology Co., Ltd., China. HNTs were under depurative and shortened treatments in terms of previous work.<sup>31</sup> PAMAM dendrimer (ethylenediamine core, generation 4.0) was obtained from Sigma-Aldrich. Toluene, succinic anhydride, *N,N*-dimethylformamide (DMF), APTES, succinic anhydride (SA), *N*-hydroxysuccinimide (NHS), and *N*-(3-(dimethylamino)propyl)-*N'*-ethylcarbodiimide (EDC), and all other chemicals were bought from Aladdin. Lipofectamine 2000 (Lipo2000) was purchased from Invitrogen. Opti-MEM reduced serum medium was obtained from Gibco. siVEGF (sense: 5'-GAUUAUGCGGAUCAACCUtt-3'), and scrambled siRNA (sense: 5'-AUCGGAGCAGUCGUAAUGCtt-3') were purchased from Guangzhou RiboBio Co.,

Ltd., China. Ultrapure water was obtained from the Milli-Q water (resistivity  $>18.2$  M $\Omega$  cm) system.

**Synthesis of PAMAM-g-HNTs.** PAMAM-g-HNTs were synthesized on the basis of references with slight modifications.<sup>31,32</sup> In brief, short HNTs (100 mg) and 3 mL of APTES were reacted in methylbenzene under magnetic stirring treatment for 12 h at 85  $^{\circ}\text{C}$ . The product was washed with ethanol and water three times and then dried at 60  $^{\circ}\text{C}$  to obtain HNTs-NH<sub>2</sub>. Afterward, HNTs-NH<sub>2</sub> (80 mg) reacted with SA in DMF solution for 24 h at room temperature to obtain HNTs-COOH. PAMAM-g-HNTs were then synthesized by reaction of HNTs-COOH (100 mg) with PAMAM (100  $\mu\text{L}$ ) with EDC and NHS as catalyst. PAMAM-g-HNTs were washed by ethanol and ultrapure water and collected using a freeze-dryer (Scientz-18ND, Ningbo Scientz Biotechnology Ltd., China).

**Characterization of PAMAM-g-HNTs.** *Fourier Transform Infrared Spectroscopy (FT-IR).* FTIR spectra were collected in FTIR instrument (Nicolet iSS0, Thermo Fisher Scientific Ltd., USA). Twenty-two consecutive scans were taken from 4000 to 400  $\text{cm}^{-1}$ .

*X-ray dDfraction (XRD).* XRD analyses were analyzed using an X-ray diffractometer (MiniFlex-600, Rigaku Corporation, Japan) from 3 $^{\circ}$  to 70 $^{\circ}$  with scanning speed of 5 $^{\circ}$ /min.

*X-ray Photoelectron Spectroscopy (XPS).* XPS analyses were tested with a XPS instrument (ESCALAB250Xi, Thermo Fisher Scientific Ltd., USA). High-resolution scanning of nitrogen and carbon elements was conducted.

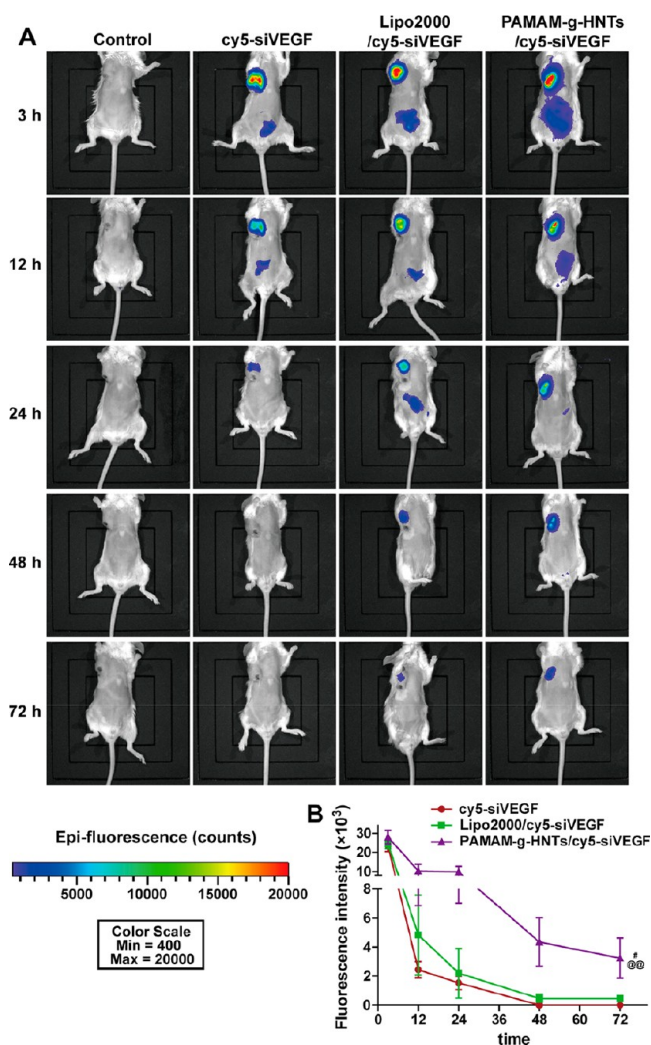


**Figure 9.** Controlled release effect of PAMAM-g-HNTs/cy5-siVEGF in vivo. (A) Cy5-siVEGF fluorescence photos of mice at 3, 12, 24, 48, and 72 h after administration of cy5-siVEGF, Lipo2000/cy5-siVEGF, PAMAM-g-HNTs/cy5-siVEGF. (B) Quantification of cy5-siVEGF fluorescence intensity in tumor tissues at indicative time points. The data are shown by mean  $\pm$  SD ( $n = 3$ ).  $^{\#}P < 0.001$  vs cy5-siVEGF;  $@@P < 0.01$  vs Lipo2000/cy5-siVEGF.

**Dynamic Light Scattering (DLS).** The size distributions of nanoparticles aqueous dispersion (0.05 wt %) were analyzed by a Nano-ZS instrument (Malvern Instruments Ltd., UK).

**$\zeta$ -Potential Analysis.** Zeta potential of nanoparticle aqueous dispersion (0.05 wt %) was measured using a Nano-ZS instrument (Malvern Instruments Ltd., UK).

**Thermogravimetric Analysis (TGA).** TGA analyses were conducted with a TGA instrument (TG209F3-ASC, Netzsch Ltd., Germany) at a heating rate of 10 °C/min under the N<sub>2</sub> atmosphere.

**Transmission Electron Microscopy (TEM).** The HNTs and PAMAM-g-HNTs ethanol dispersions (0.05 wt %) were dropped on the carbon film supported copper grids, and then dried in air. The samples were observed with a TEM instrument (JEM-2100F, JEOL Ltd., Japan), and the accelerating voltage was 100 kV.

**Atomic Force Microscopy (AFM).** AFM images were observed with a multimode AFM instrument (Bioscope Catylyst Nanoscope-V, Broker Instruments Ltd., USA).

Tap150-Al-G silicon AFM probes (budgets sensors) was used to capture AFM images in ScanAsyst mode (scanning speed was 0.6 Hz,  $k = 5$  N/m, and resonance frequency was 150 kHz). The experiment was handled at room temperature.

**Barrett–Joyner–Halenda (BJH) Pore Analysis.** BJH pore analysis was conducted by automated surface area and pore size analyzer (BeiShiDe 3H-2000, Instrument-S & T.Co., Ltd., China).

**Cells and Cell Culture Conditions.** Human umbilical vein endothelial cells (HUVECs), human breast adenocarcinoma cell line (MCF-7), and mouse breast cancer cells (4T1) were obtained from the Laboratory Animal Center of Sun Yat-Sen University. Cells were cultured in Dulbecco's modified Eagle medium (DMEM, Gibco) containing 1% penicillin/streptomycin and 10% fetal bovine serum (FBS, Gibco) in a humid incubator with 5% CO<sub>2</sub> at 37 °C.

**Cytotoxicity Assay.** Cell counting kit-8 (CCK-8) assay was used to evaluate the cytotoxicity. HUVECs and MCF-7 cells were seeded in 96-well plates ( $8 \times 10^3$  cells/well), and then incubated with PAMAM-g-HNTs at different concentrations for 24 h. Cells were washed with fresh PBS and replaced with 100  $\mu$ L of DMEM medium. The OD value at 450 nm was measured using a microplate reader (Multiskan MK3, Thermo Fisher Scientific Ltd., USA) after incubated with 10  $\mu$ L of CCK-8 reagents (BestBio Biotechnology Ltd., China) for 4 h. PBS was designed as the control group. Cell viability was calculated as the ratio of the sample and the control group.

**Gel Electrophoresis.** Agarose gel electrophoresis assay was designed to examine the siRNA binding affinity. A constant amount of 0.6  $\mu$ g siRNA was used. 0.6 g agarose was dissolved into 60 mL of TAE buffer to form agarose gel, and then PAMAM-g-HNTs/siRNA complexes were added. 3  $\mu$ L of ethidium bromide was used as eikonogen. The artifactitious agarose gel was conducted at 100 V for 25 min in TAE buffer and then photographed through an UV illumination (CUV-10, Qin Xiang Scientific Instrument Co., Ltd., Shanghai).

**In Vitro Cellular Uptake Studies.** MCF-7 cells with density of  $8 \times 10^4$  cells/well were cultured in 12-well plates for 24 h. Then PAMAM-g-HNTs and cy3-siRNA (20, 40, 60, and 80 nM) in 1 mL of Opti-MEM reduced serum medium (Thermo Fisher Scientific Ltd., USA) were added into the wells at weight ratio of 80. Lipo2000 loaded with 60 nM cy3-siRNA was designed as control group. After incubation for 6 h, the cells were washed with fresh PBS and collected in 300  $\mu$ L of PBS for flow cytometry (BD FACSCanto, USA) measurement.

The uptake of PAMAM-g-HNTs/siRNA (weight ratio was 20, 40, and 80) was investigated. MCF-7 cells ( $8 \times 10^4$  cells/well) were cultured in 12-well plates for 24 h. Then, PAMAM-g-HNTs/cy3-siRNA complexes were added into the wells and kept for 6 h. The concentration of siRNA was 60 nM. Afterward, cells were suspended in PBS and analyzed with flow cytometry.

**Endosomal/Lysosomal Escape.** MCF-7 cells ( $1 \times 10^4$  cells/dish) were cultured in a confocal dish (NEST, China) for 24 h prior to the experiment. Then, PAMAM-g-HNTs/cy3-siRNA complexes (weight ratio was 80, and the concentration of siRNA was 60 nM) in 1 mL of Opti-MEM reduced serum medium were incubated with cells at 37 °C for another 4 and 6 h. The cells were then washed with PBS three times, then stained using LysoTracker green and DAPI solutions, and

observed with a confocal laser scanning microscope (CLSM880, Carl Zeiss AG, Germany).

**In Vitro Gene Silencing Effects.** MCF-7 cells were seeded in 6-well plates ( $2 \times 10^5$  cells/well) for 24 h. Then Opti-MEN reduced serum media containing siVEGF, PAMAM-g-HNTs/Scram, Lipo2000/siVEGF, and PAMAM-g-HNTs/siVEGF were added in the wells. siRNA concentration was equivalent to 60 nM. After incubation with cells for 6 h, the culture medium was replaced with free DMEM culture medium. The cellular levels of VEGF mRNA and protein were evaluated by Western blot and qRT-PCR after 48 h.

Trizol (Invitrogen, USA) was used to extract RNA from the cells. DNase (Promega, USA) was used to remove the genome in the RNA. The reaction mixture was digested at 37 °C and inactivated at 65 °C. The OD value of RNA was measured with biophotometer plus nucleic acid protein analyzer (Eppendorf BioPhotometer D30, Germany). SYBR Green qPCR SuperMix (Invitrogen, USA) was used to conduct the qRT-PCR analysis, and the data were analyzed with Sequence Detection System (ABI PRISM7500, USA). GAPDH served as the endogenous control.

The primers used in the PCR are as follows: siVEGF-forward: 5'-CCCCGACGAGATAGAGTACA-3'. siVEGF-reverse: 5'-CGCTTTCGTTTTTGGACCTT-3'. GAPDH-forward: 5'-GGCCTCCAAGGAGTAAGAAA-3'. GAPDH-reverse: 5'-GCCCTCCTGTTATTATGG-3'.

For the Western blot analysis, transfected MCF-7 cells were washed with PBS and then suspended in 100  $\mu$ L of lysis buffer. The lysates were newly prepared and conducted by SDS-PAGE gel electrophoresis at 80 V for 50 min, and then analyzed by Western blot with primary VEGF antibody (SC-7269, Santa Cruz Biotechnology Ltd., USA) and second antibody (Rabbit Anti-Mouse IgG (H+L), Southern Biotech Ltd., USA) at dilution of 1:1000. GAPDH (KC-5GS, Shanghai Kangcheng biological Ltd., China) served as the endogenous control and the software Quantity One v 4.6.7 was applied to measure the VEGF protein expression levels quantitatively.

**Cell Apoptosis Assay.** MCF-7 cells ( $2 \times 10^5$  cells/well) were seeded in 6-well plates for 24 h. Opti-MEN reduced serum medium containing siVEGF, PAMAM-g-HNTs/Scram, Lipo2000/siVEGF, and PAMAM-g-HNTs/siVEGF were added in the wells for 6 h subsequently with siRNA concentration of 60 nM. The transfected liquid was replaced with free DMEM culture medium. After transfection for 48 h, the apoptosis of cells was detected with flow cytometry after treating with the Annexin V-FITC/PI apoptosis detection kit (eBioscience, Thermo Fisher Scientific Ltd., USA). The data were analyzed with Flowjo software (v10.4, Tree Star, Inc., USA). AO/EB staining assay was also used for determine cell apoptosis of MCF-7 cells. Similar to the former procedures, acridine orange/ethidium bromide (AO/EB) was used to stain cells into red/green ones, and then photographed with a fluorescence microscope (XDY-2, Liss Optical Instrument Ltd., China).

**Animal Feeding Conditions.** Female BALB/c mice (7 weeks old) weighting 18–22 g were purchased from Guangdong Medical Laboratory Animal Center (Guangzhou, China). All mice were maintained under specific pathogen-free conditions ( $23 \pm 1$  °C) with a 12 h dark–light cycle and allowed to access standard water and diet. The animals were allowed to acclimatize to the environment for a week before the experiment. All animal care and experimental procedures

were conducted following the National Institutes of Health's Guide for the Care and Use of Laboratory Animals.

**Antitumor Efficacy and Systemic Toxicity in 4T1-Bearing Mice.** 4T1-bearing mice were divided into five groups randomly ( $n = 6$  for each): control, PAMAM-HNTs/Scram, siVEGF, Lipo/siVEGF, and PAMAM-HNTs/siVEGF after injection of 4T1 cell suspension when the tumor volumes grew to  $\sim 100$  mm<sup>3</sup>. The amount of siRNA in each intratumoral injection was set at a dose of 0.7 mg/kg and conducted every 3 days for 15 days. Body weight of mice was measured every day, tumor size was measured every 3 days, and tumor volume was calculated as followings:

$$\text{Volume}(\text{mm}^3) = 0.5 \times [\text{length}(\text{mm})] \times [\text{width}(\text{mm})]^2$$

Mice were sacrificed with diethyl ether and tumor tissues were collected, weighed, and photographed immediately at the end of treatment. The tumor inhibition rate was calculated as following formulas:

$$\begin{aligned} &\text{Tumor inhibition} \\ &= \left( \frac{\text{tumor weight}_{\text{control group}} - \text{tumor weight}_{\text{experiment group}}}{\text{tumor weight}_{\text{control group}}} \right) \\ &\times 100\% \end{aligned}$$

Tumor tissues were sectioned after 4% paraformaldehyde fixed, paraffin embedded for hematoxylin and eosin (H&E) staining, the terminal deoxynucleotidyl transferase dUTP nick end labeling (TUNEL) assay and immunohistochemical (IHC) were analyzed according to manufacturer's instructions. TUNEL positive cells were quantified and represented as percentages of the total number of cells in 5 randomly selected fields. The integrated optical density value was calculated by using ImageJ (v 2.1.4.7, National Institutes of Health, USA) software. As for the histological analysis, the heart, spleen, lung, and kidney of mice were also collected at day 15 and sectioned with the description above for H&E staining.

**In Vivo Imaging Studies.** When the volumes of tumor in mice grew to  $\sim 100$  mm<sup>3</sup>, cy5-siVEGF, Lipo2000/cy5-siVEGF, and PAMAM-g-HNTs/cy5-siVEGF (0.7 mg of siVEGF equiv/kg) were intratumorally injected into the mice, respectively. The cy5-siVEGF distribution within tumor tissues was detected and analyzed by an in vivo fluorescence imaging system (IVISSpectrum BL, PerkinElmer, USA) at 3, 12, 24, 48, and 72 h post-injection.

**Statistical Analysis.** Data were given as mean  $\pm$  standard deviation and analyzed by one-way analysis of variance (ANOVA) and a Tukey post hoc test through the software of GraphPad Prism 6 (GraphPad Software Inc., USA).  $P < 0.05$  was considered statistically significant.

## ■ ASSOCIATED CONTENT

### 📄 Supporting Information

The Supporting Information is available free of charge on the ACS Publications website at DOI: 10.1021/acs.bioconjchem.8b00321.

Determination of primary amine content by TNBS assay, Zeta potential of HNTs-NH<sub>2</sub> and HNTs-COOH, BJH pore distribution of HNTs and PAMAM-g-HNTs (PDF)

## AUTHOR INFORMATION

### Corresponding Authors

\*E-mail: rongronghe@jnu.edu.cn.

\*E-mail: liumx@jnu.edu.cn. Tel: (86) 20-85226663. Fax: (86) 20-85223271.

### ORCID

Mingxian Liu: 0000-0002-5466-3024

### Author Contributions

#Zheru Long and Yan-Ping Wu contributed equally to this work.

### Notes

The authors declare no competing financial interest.

## ACKNOWLEDGMENTS

This work was financially supported by National High Technology Research and Development Program of China (2015AA020915), the National Natural Science Foundation of China (grant No. 51473069, 81622050, and 51502113), and the Guangdong Natural Science Funds for Distinguished Young Scholar (grant No. S2013050014606), Science and Technology Program of Guangzhou, China (No. 2013J4100100), Guangdong Special Support Program (2014TQ01C127 and 2014TQ01R229), the Pearl River S&T Nova Program of Guangzhou (201610010026), and Guangdong Province Ocean and Fisheries Bureau-Key Technology Research and Development Program (A201701A02).

## ABBREVIATIONS

HNTs, halloysite nanotubes; PAMAM, polyamidoamine; PAMAM-g-HNTs, polyamidoamine grafted halloysite nanotubes; siRNA, small interfering RNA; siVEGF, small interfering vascular endothelial growth factor; AuNPs, gold nanoparticles; GO, graphene oxide; PEI, polyethylenimine; CNTs, carbon nanotubes; APTES, 3-aminopropyltriethoxysilane; PEI-g-HNTs, PEI grafted short HNTs; Lipo2000, Lipofectamine 2000; TNBS, 2,4,6-trinitrobenzenesulfonic acid

## REFERENCES

- Hannon, G. J. (2002) RNA interference. *Nature* 418, 244–251.
- He, H., Zheng, N., Song, Z., Kim, K. H., Yao, C., Zhang, R., Zhang, C., Huang, Y., Uckun, F. M., and Cheng, J. (2016) Suppression of hepatic inflammation via systemic siRNA delivery by membrane-disruptive and endosomolytic helical polypeptide hybrid nanoparticles. *ACS Nano* 10, 1859–1870.
- Nelson, C. E., Kim, A. J., Adolph, E. J., Gupta, M. K., Yu, F., Hocking, K. M., Davidson, J. M., Guelcher, S. A., and Duvall, C. L. (2014) Tunable delivery of siRNA from a biodegradable scaffold to promote angiogenesis *In Vivo*. *Adv. Mater.* 26, 607–614.
- Li, J., Yu, X., Wang, Y., Yuan, Y., Xiao, H., Cheng, D., and Shuai, X. (2014) A reduction and pH dual-sensitive polymeric vector for long-circulating and tumor-targeted siRNA delivery. *Adv. Mater.* 26, 8217–8224.
- Tomar, R. S., Matta, H., and Chaudhary, P. M. (2003) Use of adeno-associated viral vector for delivery of small interfering RNA. *Oncogene* 22, 5712–5715.
- Zhang, J., Li, X., and Huang, L. (2014) Non-viral nanocarriers for siRNA delivery in breast cancer. *J. Controlled Release* 190, 440–450.
- Yin, H., Kanasty, R. L., Eltoukhy, A. A., Vegas, A. J., Dorkin, J. R., and Anderson, D. G. (2014) Non-viral vectors for gene-based therapy. *Nat. Rev. Genet.* 15, 541–555.

(8) Zhang, L., Zheng, W., Tang, R., Wang, N., Zhang, W., and Jiang, X. (2016) Gene regulation with carbon-based siRNA conjugates for cancer therapy. *Biomaterials* 104, 269–278.

(9) Figueroa, E. R., Lin, A. Y., Yan, J., Luo, L., Foster, A. E., and Drezek, R. A. (2014) Optimization of PAMAM-gold nanoparticle conjugation for gene therapy. *Biomaterials* 35, 1725–1734.

(10) Feng, Y., Hu, K., Chen, Y., Yu, M., Wang, D., Wang, Q., Yong, K. T., Fei, L., Liang, Y., and Li, Z. (2017) SiRNA delivery with PEGylated graphene oxide nanosheets for combined photothermal and gene therapy for pancreatic cancer. *Theranostics* 7, 1133–1148.

(11) Chen, Q., Meng, X., Zheng, W., Xu, T., Hong, D., and Jie, L. (2017) Se/Ru-decorated porous metal-organic framework nanoparticles for the delivery of pooled siRNAs to reversing multidrug resistance in taxol-resistant breast cancer cells. *ACS Appl. Mater. Interfaces* 9, 6712–6724.

(12) Caoduro, C., Hervouet, E., Girardthermier, C., Gharbi, T., Boulahdour, H., Delagemourroux, R., and Pudlo, M. (2017) Carbon nanotubes as gene carriers: Focus on internalization pathways related to functionalization and properties. *Acta Biomater.* 49, 36–44.

(13) Yamaguchi, H., Tsuchimochi, M., Hayama, K., Kawase, T., and Tsubokawa, N. (2016) Dual-labeled near-infrared/99mTc imaging probes using PAMAM-coated silica nanoparticles for the imaging of HER2-expressing cancer cells. *Int. J. Mol. Sci.* 17, 1086–1101.

(14) Shi, Y.-F., Tian, Z., Zhang, Y., Shen, H.-B., and Jia, N.-Q. (2011) Functionalized halloysite nanotube-based carrier for intracellular delivery of antisense oligonucleotides. *Nanoscale Res. Lett.* 6, 608.

(15) Wu, H., Shi, Y., Huang, C., Zhang, Y., Wu, J., Shen, H., and Jia, N. (2014) Multifunctional nanocarrier based on clay nanotubes for efficient intracellular siRNA delivery and gene silencing. *J. Biomater. Appl.* 28, 1180–1189.

(16) Lvov, Y. M., Shchukin, D. G., Möhwald, H., and Price, R. R. (2008) Halloysite clay nanotubes for controlled release of protective agents. *ACS Nano* 2, 814–20.

(17) Liu, M., Jia, Z., Jia, D., and Zhou, C. (2014) Recent advance in research on halloysite nanotubes-polymer nanocomposite. *Prog. Polym. Sci.* 39, 1498–1525.

(18) Liu, M., Zhang, Y., Wu, C., Xiong, S., and Zhou, C. (2012) Chitosan/halloysite nanotubes bionanocomposites: structure, mechanical properties and biocompatibility. *Int. J. Biol. Macromol.* 51, 566–75.

(19) Kryuchkova, M., Danilushkina, A., Lvov, Y., and Fakhrullin, R. (2016) Evaluation of toxicity of nanoclays and graphene oxide in vivo: a paramecium caudatum study. *Environ. Sci.: Nano* 3, 442–452.

(20) Abdullayev, E., and Lvov, Y. (2010) Clay nanotubes for corrosion inhibitor encapsulation: release control with end stoppers. *J. Mater. Chem.* 20, 6681–6687.

(21) Ye, F., Zhao, D., Yao, P., Wang, W., Zhang, L., and Lvov, Y. (2015) Highly aging-resistant elastomers doped with antioxidant-loaded clay nanotubes. *ACS Appl. Mater. Interfaces* 7, 8156–8165.

(22) Jing, H., Higaki, Y., Ma, W., Wu, H., Yah, W. O., Otsuka, H., Lvov, Y. M., and Takahara, A. (2013) Internally modified halloysite nanotubes as inorganic nanocontainers for a flame retardant. *Chem. Lett.* 42, 121–123.

(23) Lvov, Y., Wang, W., Zhang, L., and Fakhrullin, R. (2016) Halloysite clay nanotubes for loading and sustained release of functional compounds. *Adv. Mater.* 28, 1227–1250.

(24) Massaro, M., Lazzara, G., Milioto, S., Noto, R., and Riela, S. (2017) Covalently modified halloysite clay nanotubes: synthesis, properties, biological and medical applications. *J. Mater. Chem. B* 5, 2867–2882.

(25) Darrat, Y., Naumenko, E., Cavallaro, G., Lazzara, G., Lvov, Y., and Fakhrullin, R. (2018) Tubular nanocontainers for drug delivery. *Nanoarchitectonics*, 85–108.

(26) Massaro, M., Amorati, R., Cavallaro, G., Guernelli, S., Lazzara, G., Milioto, S., Noto, R., Poma, P., and Riela, S. (2016) Direct chemical grafted curcumin on halloysite nanotubes as dual-responsive prodrug for pharmacological applications. *Colloids Surf., B* 140, 505–513.

- (27) Dзамukova, M. R., Naumenko, E. A., Lvov, Y. M., and Fakhrullin, R. F. (2015) Enzyme-activated intracellular drug delivery with tubule clay nanoformulation. *Sci. Rep.* 5, 10560.
- (28) Tan, D., Yuan, P., Annabi-Bergaya, F., Liu, D., Wang, L., Liu, H., and He, H. (2014) Loading and in vitro release of ibuprofen in tubular halloysite. *Appl. Clay Sci.* 96, 50–55.
- (29) Liu, M., Chang, Y., Yang, J., You, Y., He, R., Chen, T., and Zhou, C. (2016) Functionalized halloysite nanotube by chitosan grafting for drug delivery of curcumin to achieve enhanced anticancer efficacy. *J. Mater. Chem. B* 4, 2253–2263.
- (30) Yang, J., Wu, Y., Shen, Y., Zhou, C., Li, Y. F., He, R. R., and Liu, M. (2016) Enhanced therapeutic efficacy of doxorubicin for breast cancer using chitosan oligosaccharide-modified halloysite nanotubes. *ACS Appl. Mater. Interfaces* 8, 26578–26590.
- (31) Long, Z., Zhang, J., Shen, Y., Zhou, C., and Liu, M. (2017) Polyethyleneimine grafted short halloysite nanotubes for gene delivery. *Mater. Sci. Eng., C* 81, 224–235.
- (32) Kurczewska, J., Ceglowski, M., Messyasz, B., and Schroeder, G. (2018) Dendrimer-functionalized halloysite nanotubes for effective drug delivery. *Appl. Clay Sci.* 153, 134–143.
- (33) Dementjev, A., De Graaf, A., Van de Sanden, M., Maslakov, K., Naumkin, A., and Serov, A. (2000) X-ray photoelectron spectroscopy reference data for identification of the C 3 N 4 phase in carbon–nitrogen films. *Diamond Relat. Mater.* 9, 1904–1907.
- (34) Li, Y., He, W., Liu, J., Sheng, F., Hu, Z., and Chen, X. (2005) Binding of the bioactive component jatrorrhizine to human serum albumin. *Biochim. Biophys. Acta, Gen. Subj.* 1722, 15–21.
- (35) Simons, W. W. (1978) *Sadtler handbook of infrared spectra*; Sadtler Research Laboratories.
- (36) Wu, Y.-P., Yang, J., Gao, H.-Y., Shen, Y., Jiang, L., Zhou, C., Li, Y.-F., He, R.-R., and Liu, M. (2018) Folate-conjugated halloysite nanotubes, an efficient drug carrier, deliver doxorubicin for targeted therapy of breast cancer. *ACS Appl. Nano Mater.* 1, 595–608.
- (37) Liu, M., Guo, B., Du, M., Cai, X., and Jia, D. (2007) Properties of halloysite nanotube–epoxy resin hybrids and the interfacial reactions in the systems. *Nanotechnology* 18, 455703.
- (38) Wu, Y., Yang, J., Gao, H., Shen, Y., Jiang, L., Zhou, C., Li, Y., He, R., and Liu, M. (2018) Folate-conjugated halloysite nanotubes, an efficient drug carrier, deliver doxorubicin for targeted therapy of breast cancer. *ACS Appl. Nano Mater.* 1, 595–608.
- (39) Liu, M., Wu, C., Jiao, Y., Xiong, S., and Zhou, C. (2013) Chitosan–halloysite nanotubes nanocomposite scaffolds for tissue engineering. *J. Mater. Chem. B* 1, 2078–2089.
- (40) Kesharwani, P., Banerjee, S., Gupta, U., Mohd Amin, M. C. I. M., Padhye, S., Sarkar, F. H., and Iyer, A. K. (2015) PAMAM dendrimers as promising nanocarriers for RNAi therapeutics. *Mater. Today* 18, 565–572.
- (41) Nussbaumer, M. G., Duskey, J. T., Rother, M., Renggli, K., Chami, M., and Bruns, N. (2016) Chaperonin-dendrimer conjugates for siRNA delivery. *Adv. Sci.* 3, 1600046.
- (42) Putnam, D., Gentry, C. A., Pack, D. W., and Langer, R. (2001) Polymer-based gene delivery with low cytotoxicity by a unique balance of side-chain termini. *Proc. Natl. Acad. Sci. U. S. A.* 98, 1200–1205.
- (43) Cai, X., Zhu, H., Zhang, Y., and Gu, Z. (2017) Highly efficient and safe delivery of VEGF siRNA by bioreducible fluorinated peptide dendrimers for cancer therapy. *ACS Appl. Mater. Interfaces* 9, 9402–9415.
- (44) Ferrara, N., Gerber, H.-P., and LeCouter, J. (2003) The biology of VEGF and its receptors. *Nat. Med.* 9, 669–676.
- (45) <https://www.proteinatlas.org/ENSG00000112715-VEGFA/cell>.
- (46) Kim, S. H., Jeong, J. H., Lee, S. H., Kim, S. W., and Park, T. G. (2008) Local and systemic delivery of VEGF siRNA using polyelectrolyte complex micelles for effective treatment of cancer. *J. Controlled Release* 129, 107–116.
- (47) Ku, S. H., Kim, K., Choi, K., Kim, S. H., and Kwon, I. C. (2014) Tumor-targeting multifunctional nanoparticles for siRNA delivery: recent advances in cancer therapy. *Adv. Healthcare Mater.* 3, 1182–1193.
- (48) Yue, Q., Shao, Z., Chang, S., and Li, J. (2013) Adsorption of gas molecules on monolayer MoS<sub>2</sub> and effect of applied electric field. *Nanoscale Res. Lett.* 8, 425.
- (49) Varkouhi, A. K., Foillard, S., Lammers, T., Schifflers, R. M., Doris, E., Hennink, W. E., and Storm, G. (2011) siRNA delivery with functionalized carbon nanotubes. *Int. J. Pharm.* 416, 419–425.
- (50) Foillard, S., Zuber, G., and Doris, E. (2011) Polyethylenimine-carbon nanotube nanohybrids for siRNA-mediated gene silencing at cellular level. *Nanoscale* 3, 1461–1464.
- (51) Esfand, R., and Tomalia, D. A. (2001) Poly (amidoamine)- (PAMAM) dendrimers: from biomimicry to drug delivery and biomedical applications. *Drug Discovery Today* 6, 427–436.
- (52) Zheng, W., Cao, C., Liu, Y., Yu, Q., Zheng, C., Sun, D., Ren, X., and Liu, J. (2015) Multifunctional polyamidoamine-modified selenium nanoparticles dual-delivering siRNA and cisplatin to A549/DDP cells for reversal multidrug resistance. *Acta Biomater.* 11, 368–380.
- (53) Holash, J., Wiegand, S., and Yancopoulos, G. (1999) New model of tumor angiogenesis: dynamic balance between vessel regression and growth mediated by angiopoietins and VEGF. *Oncogene* 18, 5356–5362.
- (54) Toi, M., Inada, K., Suzuki, H., and Tominaga, T. (1995) Tumor angiogenesis in breast cancer: its importance as a prognostic indicator and the association with vascular endothelial growth factor expression. *Breast Cancer Res. Treat.* 36, 193–204.
- (55) Folkman, J. (2003) Angiogenesis and apoptosis. *Semin. Cancer Biol.* 13, 159–167.
- (56) Maeda, H., Wu, J., Sawa, T., Matsumura, Y., and Hori, K. (2000) Tumor vascular permeability and the EPR effect in macromolecular therapeutics: a review. *J. Controlled Release* 65, 271–284.
- (57) Li, Y., Liu, R., Shi, Y., Zhang, Z., and Zhang, X. (2015) Zwitterionic poly (carboxybetaine)-based cationic liposomes for effective delivery of small interfering RNA therapeutics without accelerated blood clearance phenomenon. *Theranostics* 5, 583–596.